



# Cyto/hemocompatible magnetic hybrid nanoparticles ( $\text{Ag}_2\text{S}-\text{Fe}_3\text{O}_4$ ) with luminescence in the near-infrared region as promising theranostic materials



Ibrahim Hocaoglu<sup>a</sup>, Didar Asik<sup>b</sup>, Gulen Ulusoy<sup>c</sup>, Christian Grandfil<sup>d</sup>, Isaac Ojea-Jimenez<sup>e</sup>, François Rossi<sup>e</sup>, Alper Kiraz<sup>a,f</sup>, Nurcan Doğan<sup>g</sup>, Havva Yagci Acar<sup>a,c,\*</sup>

<sup>a</sup> Materials Science and Engineering, Koc University, Istanbul 34450, Turkey

<sup>b</sup> Department of Molecular Biology and Genetics, Koc University, Istanbul 34450, Turkey

<sup>c</sup> Department of Chemistry, Koc University, Istanbul 34450, Turkey

<sup>d</sup> Center Interfacultaire des Biomateriaux, University of Liege, Liege B 4000, Belgium

<sup>e</sup> Institute of Health and Consumer Protection, European Commission Joint Research Center, Ispra 21027, Italy

<sup>f</sup> Department of Physics, Koc University, Istanbul 34450, Turkey

<sup>g</sup> Department of Physics, Gebze Technical University, Gebze, Turkey

## ARTICLE INFO

### Article history:

Received 17 March 2015

Received in revised form 13 May 2015

Accepted 29 May 2015

Available online 11 June 2015

### Keywords:

Hybrid nanoparticles

Near-infrared

Silver sulfide

Quantum dot

Magnetic nanoparticle

## ABSTRACT

Small hybrid nanoparticles composed of highly biocompatible  $\text{Ag}_2\text{S}$  quantum dots (QD) emitting in the near-infrared region and superparamagnetic iron oxide (SPION) are produced in a simple extraction method utilizing ligand exchange mechanism. Hybrid nanoparticles luminesce at the same wavelength as the parent QD, therefore an array of hybrid nanoparticles with emission between 840 and 912 nm were easily produced. Such hybrid structures have (1) strong luminescence in the medical imaging window eliminating the autofluorescence of cells as effective optical probes, (2) strong magnetic response for magnetic targeting and (3) good cyto/hemocompatibility. An interesting size dependent cytotoxicity behavior was observed in HeLa and NIH/3T3 cell lines: smallest particles are internalized significantly more by both of the cell lines, yet showed almost no significant cytotoxicity in HeLa between 10 and 25  $\mu\text{g}/\text{mL}$  Ag concentration but were most toxic in NIH/3T3 cells. Cell internalization and hence the cytotoxicity enhanced when cells were incubated with the hybrid nanoparticles under magnetic field, especially with the hybrid nanoparticles containing larger amounts of SPION in the hybrid composition. These results prove them as effective optical imaging agents and magnetic delivery vehicles. Combined with the known advantages of SPIONs as a contrast agent in MRI, these particles are a step forward for new theranostics for multimode imaging and magnetic targeting.

© 2015 Elsevier B.V. All rights reserved.

## 1. Introduction

Multifunctional colloidal nanoparticles are of special interest for medicine and biotechnology. Superparamagnetic iron oxide nanoparticles (SPIONs) [1–4] and luminescent semiconductor quantum dots (QDs) [5–7] have been widely studied for medical and biological applications such as diagnostics, therapy and labeling. SPIONs have been particularly utilized as contrast agents in MRI for both vascular and organ imaging [2,3]. Magnetic separation

is another application that has reached commercialization in biotechnology [8,9]. Cell tracking [10], magnetic drug delivery, hyperthermia [8,9], detoxification [11], etc. are the other applications of SPIONs which are in the research or clinical phase.

QDs are replacing organic fluorophores in biological applications with high extinction coefficient and enhanced photo-stability [12–17]. They possess broad absorption and narrow emission profiles allowing excitation of different QDs at a single wavelength with minimal overlap of emission [7,18]. Size tunable emission due to quantum confinement allows production of QDs with same composition but with different emission wavelength. Emission can be tuned within the visible region with QDs composed of group II–VI elements (*i.e.* Cd-chalcogenides) or within NIR by using QDs composed of group IV–VI (*i.e.* Pb-chalcogenides) elements.

\* Corresponding author at: Materials Science and Engineering, Koc University, Istanbul 34450, Turkey. Tel.: +90 2123381742.  
E-mail address: [fyagci@ku.edu.tr](mailto:fyagci@ku.edu.tr) (H.Y. Acar).

Complex nanoparticles are being fabricated recently, such as  $\text{Fe}_3\text{O}_4/\text{SiO}_2/\text{graphene}/\text{CdTe}$  chitosan [19]. Hybrid nanomaterials comprising magnetic nanoparticles are of great interest for dual imaging such as MRI-CT [20] or MRI-SPECT [21], which were achieved by  $\text{Au}-\text{Fe}_3\text{O}_4$  and  $\text{Fe}_3\text{O}_4-\text{Ag}^{125}\text{I}$ , respectively, and requires difficult synthesis protocols. Magnetic-luminescent hybrid nanoparticles composed of SPIONs and QDs are highly attractive multifunctional materials since they offer opportunity for dual imaging, sensing-separation, imaging-therapy and multiplexed sensors. Response of SPIONs to external magnetic field has been widely utilized to target nanoparticles to the site of interest (e.g. tumors) and enhance their internalization which increases the therapeutic effect and decreases potential side effects [18,22]. Such hybrid nanoparticles could therefore be targeted via magnetic manipulation. Also, combinations of imaging modalities are desirable. Optical imaging utilizing QDs has a benefit of sensitivity but lacks resolution and has depth limitation, whereas MRI offers high resolution at any depth but lacks sensitivity [23]. Combination of the two in a single entity can produce a synergistic effect and provide both sensitivity and high resolution in medical imaging. Also, real time imaging of theranostic nanoparticles and monitoring the outcome of the therapy via optical means are valuable during treatment.

Examples in the literature usually utilize Cd-chalcogenide QDs, which are the most studied and commercially available ones [24,25]. In addition to well-known toxicity of Cd-chalcogenides [26], excitation in the UV and emission in the visible region are important drawbacks of the Cd-based QDs due to intrinsic absorption, autofluorescence, scattering of the tissue, and limited penetration depth. Therefore, emission in the NIR, especially 700–900 nm range is accepted as the medical window for optical imaging [27,28]. Another practical and important drawback of combining SPIONs with materials that are luminescent in the visible region is the strong absorption of SPIONs in this wavelength range. This causes absorption of part of the photons emitted from QDs by SPIONs, hence reduce the overall quantum yield (QY) of the hybrid nanoparticles [29]. Use of Gd-species (T1 agents in the MRI) instead of SPIONs is one of the most recent solutions to this problem [23]. C-dot/SPION structures [30], upconverting  $\text{NaYF}_4$  and  $\text{NaYF}_4:\text{Yb}/\text{Er}$  combined with Gd/SPION coated with PEG [31] are some other examples to alternative hybrid systems.

Here, we propose and demonstrate an alternative composition that consists of SPIONs and  $\text{Ag}_2\text{S}$  QDs that are luminescent in the medical window.  $\text{Ag}_2\text{S}$  QDs have a band gap of 0.9 eV and they can be excited with visible light and emit in the near-infrared region (NIR). Besides,  $\text{Ag}_2\text{S}$  QDs are highly cytocompatible even without PEGylation and used for *in vitro* and *in vivo* imaging [32–35]. Such a combination offers many advantages over existing hybrid compositions in medical/biotechnology applications: (1) Excitation in the visible region, (2) no autofluorescence from the natural biological components in the NIR, (3) increased penetration depth, (4) reduced or no absorption of emitted photons by SPIONs, (5) enhanced cytocompatibility, (6) multimodality: optical and magnetic resonance imaging where neither modality (optical and magnetic) pose ionizing radiation, imaging, magnetic targeting and hyperthermia. With this motivation, we demonstrate here the synthesis of  $\text{Fe}_3\text{O}_4-\text{Ag}_2\text{S}$  superparamagnetic-luminescent hybrid nanoparticles utilizing a simple single step ligand exchange procedure in which lauric acid (LA) coating of SPIONs are exchanged with the carboxylic acid groups residing on the surface of 2-mercaptopropionic acid coated  $\text{Ag}_2\text{S}$  NIRQDs. Both LA-SPIONs and 2MPA- $\text{Ag}_2\text{S}$  NIRQDs were prepared according to our previously published methods [29,32]. Another important advantage of this system is the high quantum yield (up to 30% with respect to LDS 798 NIR dye) of the 2MPA- $\text{Ag}_2\text{S}$  NIRQDs. To the best of our knowledge, this is the highest QY reported for  $\text{Ag}_2\text{S}$  QDs until now and therefore

offers a great advantage in deep tissue imaging. As reported by Won et al., improvement of QY is much more efficient than increased concentration in enhancing the signal/noise ratio and the imaging depth [36].

Hybrids emitting at different wavelengths were obtained with good luminescence, magnetic response and outstanding colloidal stability. A detailed size and composition analysis were performed. Hybrid nanoparticles were evaluated as optical imaging agents *in vitro*. Cytocompatibility of these hybrids and cell internalization were studied in HeLa and NIH/3T3 cells. Potential of the hybrid nanoparticles in magnetic targeting was evaluated *in vitro* via cell toxicity studies conducted under magnetic field. In addition, hemocompatibility of the hybrid nanoparticles and the relevant QDs, SPIONs and the coating materials were also evaluated. Although studied less as a routine evaluation of nanoparticles, determination of hemocompatibility is crucial to understand the real *in vivo* potential of any blood contacting material due to possible toxicological reactions, such as embolization, hemolysis, cellular activation, coagulation, complement activation, fibrinolysis, etc. Compared to the animal cell toxicity assays, reactivity of blood is definitely more sensitive, taking into account that blood biological cascades can be activated by chemical groups residing on the surface of the nanomaterial. Although there are very few reports, both  $\text{Ag}_2\text{S}$  and SPION are reported as hemocompatible materials, in general [37–39]. Therefore, hemolysis, morphology of blood cells, complement activation (C3a), and coagulation activation were studied for the evaluation of hemocompatibility of the nanoparticles.

## 2. Materials and method

### 2.1. Materials

All reagents were analytical grade or highest purity. Silver nitrate ( $\text{AgNO}_3$ ) was purchased from Sigma-Aldrich. Sodium sulfide ( $\text{Na}_2\text{S}$ ) was purchased from Alfa-Aesar. 2-Mercaptopropionic acid (2-MPA), acetic acid ( $\text{CH}_3\text{COOH}$ ), sodium hydroxide ( $\text{NaOH}$ ), iron(III)chloride hexahydrate ( $\text{FeCl}_3 \cdot 6\text{H}_2\text{O}$ ), iron(II)chloride tetrahydrate ( $\text{FeCl}_2 \cdot 4\text{H}_2\text{O}$ ), ammonia (26%), chloroform and 4% paraformaldehyde were purchased from Merck. Lauric acid (LA) was purchased from Fluka. LDS 798 Near-IR laser dye was purchased from Exciton Inc. 4',6-Diamidino-2-phenylindole (DAPI) was purchased from Sigma-Aldrich.

### 2.2. Preparation of $\text{Ag}_2\text{S}-\text{Fe}_3\text{O}_4$ hybrid nanoparticles

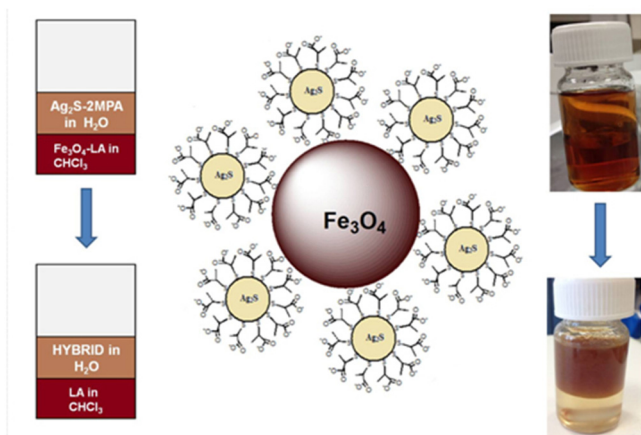
2-MPA coated  $\text{Ag}_2\text{S}$  NIRQDs were synthesized as described in the literature [32]. Lauric acid coated iron oxide nanoparticles were prepared as described by Acar et al. [29].

LA coated SPIONs in chloroform (dark brown) and  $\text{Ag}_2\text{S}$ -2MPA NIRQDs in water (brown) were mixed (equal volumes) in a round bottomed flask, sonicated briefly at room temperature and stirred at 1000 rpm overnight (Picture 1). Dark brown aqueous layer was separated from colorless chloroform layer in a separatory funnel. The aqueous layer which has the  $\text{Ag}_2\text{S}/\text{Fe}_3\text{O}_4$  hybrid nanoparticles were washed through 30K cutoff Amicon-ultra centrifugal filters until no luminescence is detected in the removed water.

### 2.3. In vitro studies

#### 2.3.1. Cell culture

Human cervical carcinoma (HeLa) and mouse fibroblast cells (NIH/3T3) were cultured in complete medium DMEM, supplemented with 10% fetal bovine serum, 1% penicillin-streptomycin antibiotic solution and 4 mM L-glutamine. Both cell lines were incubated at 37 °C under 5%  $\text{CO}_2$ . Cells were detached with Trypsin-EDTA.



**Picture 1.** Preparation of hybrid nanoparticles by ligand exchange method.

### 2.3.2. Cell viability via MTT assay

NIH/3T3 and HeLa cell lines were cultured in complete DMEM culture medium overnight at a density of  $1 \times 10^4$  cells/well in 96-well plates. Then, they were treated with fresh medium containing nanoparticles at 10–50  $\mu\text{g}$  Ag/mL concentrations. In the control group, the medium was replaced with only fresh medium. After 24 h incubation, the medium was replaced with 150  $\mu\text{L}$  complete DMEM medium and 50  $\mu\text{L}$  of the MTT (3-(4,5-dimethylthiazol-2-yl)-2,5-diphenyltetrazolium bromide) solution (5 mg/mL in 1 M PBS). After 4 h incubation with MTT, medium was discarded and purple formazan product was dissolved with 200  $\mu\text{L}$  DMSO:EtOH (1:1). Mitochondrial activity of viable cells reduces MTT to formazan and therefore quantity of formazan determined by absorbance at 600 nm (ELx800 Biotek Elisa reader) is proportional to the number of viable cells. In order to eliminate errors originating from the absorbance of QDs at 600 nm, another control group with only QDs at the concentrations used in the test wells were prepared and subjected to all manipulations that the cells with QDs are exposed, except the MTT step. Absorbance of these QD control wells at 600 nm was subtracted from the absorbance of formazan measured at 600 nm in the test wells. Percent viability was reported as the average of five replicates with respect to absorbance average of control (cells with no nanoparticle).

Cells were also incubated with hybrid nanoparticles at a 25  $\mu\text{g}$  Ag/mL dose for 24 h under magnetic field using magnetic plate holder for 96-well plates (magnetopure-96 from Chemicell) and the MTT assay protocol was applied as described above.

### 2.3.3. Quantification of cellular uptake of nanoparticles

Internalization of the nanoparticles was quantified by the measurement of silver amount in the cell lysate using Genesis ICP-OES. For ICP analysis, cells were incubated with the nanoparticles in 96-well plates, as described above. After 24 h incubation, the medium was replaced with 200  $\mu\text{L}$  MilliQ water to remove un-internalized nanoparticles. 10 mL ICP-OES solutions in distilled water were prepared from each well with addition of 200  $\mu\text{L}$  nitric acid and 200  $\mu\text{L}$  sulfuric acid. Silver amount ( $\mu\text{g}/\text{mL}$ ) in cells was reported as the average of five replicates.

Statistical analysis was performed by one-way ANOVA with Tukey's multiple comparison test of the Graph Pad Prism 5 software.

### 2.3.4. Cell imaging

100,000 HeLa cells were seeded and incubated in glass bottom dishes for 18 h. Hybrid nanoparticles at 50  $\mu\text{g}/\text{mL}$  Ag<sup>+</sup> ion concentration was added to these cells in full medium and

incubated for 6 h. Cells were also treated with DAPI (20  $\mu\text{L}$ ) to stain nuclei during the incubation. Cells were washed several times with PBS buffer (at pH = 7.4) and fixed with 4% paraformaldehyde solution.

Image acquisition was done using a home-made confocal laser scanning microscope equipped with an inverted microscope frame (Nikon TE 2000U) and a 60 $\times$  (Nikon, NA = 1.49) oil immersion objective. Samples were illuminated with a 532 nm laser after reflected by a broadband 10/90 dichroic beam splitter. Emission signals were filtered by RG665 and FGL550 long pass filters and collected by Silicon APD photon counting module.

Fluorescence microscope set up was modified to image DAPI. DAPI and hybrid nanoparticles have different absorbance and emission window. Therefore samples were also excited with a 420 nm laser to record emissions both from Ag<sub>2</sub>S QDs of the hybrid nanoparticles and DAPI in the cell nuclei. Laser power was 7–10 mW before reflection from the beam splitter. Two different channels were used to monitor emission from hybrid nanoparticles and DAPI, simultaneously. Silicon APD detector was used in both channels. RG665 and FL750 long pass filters, and HQ810/90 band pass filter were placed in front of the detector in the first channel for the detection of emission originating from hybrid nanoparticles. Emission of DAPI was recorded in the second channel with FL450 long pass filter and OD 0.9 neutral density filter ( $10^{-0.9}$  transmission) placed before the detector.

### 2.3.5. Hemocompatibility studies

All tests were performed with the agreement of the local ethical committee of the Medicine Faculty of the University of Liège. Hemocompatibility tests were performed according to ISO standards (10993-4). Normal human blood from healthy volunteer donors was collected in Terumo Venosafe citrated tubes (Terumo Europe N.V., Belgium). Experiments were done within 2 h after blood collection.

Nanoparticles dispersed in PBS were diluted in whole blood in order to obtain final nanoparticle concentrations of 1, 10, and 100  $\mu\text{g}/\text{mL}$ . Samples were incubated for 15 min at 37  $^{\circ}\text{C}$  under lateral agitation (250 rpm). In the frame of this study, the following panel of tests has been performed to evaluate the hemocompatibility of the test samples: hemolysis, morphology of blood cells (smears), counting and size distribution of blood cells, complement activation (C3a), and coagulation activation through the extrinsic (PT assay) and the intrinsic pathway (APTT assay) were studied according to protocols detailed in Ref. [40].

## 2.4. Characterization methods

Absorbance spectra were taken in the range of 300–1000 nm by a Shimadzu 3600 PC UV-Vis-NIR spectrometer. Photoluminescence spectra were recorded by a homemade system consisting of a DPSS laser source working at 532 nm, a monochromator (1/8 Newport Cornerstone 130) and a silicon detector (Thorlabs PDF10A,  $1.4 \times 10^{-15}$  W/Hz<sup>1/2</sup>). Emission signals were filtered by 590 nm long pass filter and were collected in the range of 600–1100 nm. Malvern Zetasizer nano ZS was used for the determination of hydrodynamic size and Zeta potential of particles. Particle size distribution of both Ag<sub>2</sub>S-2MPA and hybrid nanoparticles were also measured by Disc Centrifuge Photosedimentometer model DC24000UHR (CPS Instruments, EU). The instrument was operated at a disc rotation speed of 22,000 rpm using an aqueous sucrose gradient (8–24%, w/w) and calibrated before each measurement using an aqueous reference solution of PVC spheres (239 nm diameter). Gradient quality was previously confirmed by running 40 nm citrate-Ag NPs as an in-house quality check.

Spectro Genesis FEE Inductively Coupled Plasma Optical Emission Spectrometer (ICP OES) was used in determination of Ag and

Fe ion concentrations in the samples. Samples were digested with concentrated  $\text{HNO}_3$  and  $\text{H}_2\text{SO}_4$  and diluted to a certain volume with deionized water. Regression curves for each element were prepared at known concentrations. All analyses were done in triplicate and the mean values were reported.

Powder form of the hybrid nanoparticles were obtained after gentle removal of water using a freeze drier (Labconco). Thermo Scientific K-Alpha XPS with Al K-alpha monochromatic radiation (1486.3 eV) was used for XPS analyses. An adhesive aluminum tape was used for holding powdered samples. 400  $\mu\text{m}$  X-ray spot size, 50.0 eV pass energy with 0.5 eV resolution was used. The base pressure and experimental pressure were below  $3 \times 10^{-9}$  mbar and about  $1 \times 10^{-7}$  mbar, respectively. C1s peak at 285.0 eV was used as the reference.

Transmission electron microscope (TEM) (JEOL 2100, Japan) analysis was performed at an accelerating voltage of 200 kV. Samples were diluted with MilliQ water and subjected to ultrasonication (10 min). A drop (4  $\mu\text{L}$ ) of this solution was placed onto ultrathin Formvar-coated 200-mesh copper grids (Tedpella Inc.) and left to dry in air. For each sample, at least 100 particles were analyzed to obtain the average size and the size distribution. Digital images were analyzed with the ImageJ software and a custom macro performing smoothing ( $3 \times 3$  or  $5 \times 5$  median filter), manual global threshold and automatic particle analysis provided by the ImageJ. The macro can be downloaded from <http://code.google.com/p/psa-macro>. The circularity filter of 0.8 was used to exclude agglomerates that occurred during drying. EDX analyses were obtained with a QUANTAX EDS detector for TEM (Bruker, USA) in automatic acquisition mode and with the same background correction.

Magnetic measurements were carried out with the Quantum Design Model 6000 vibrating sample magnetometer (QD-VSM) with an option for the physical property measurement system (PPMS). Measurements were performed between  $\pm 15$  kOe at

different temperatures (10, 100, 200, 300, 400 K). Zero field cooled (ZFC) and field cooled (FC) measurements were done at 50 Oe and blocking temperature was determined from MT measurement.

### 3. Results and discussion

#### 3.1. Synthesis, physical and chemical characterization of the hybrid nanoparticles ( $\text{Ag}_2\text{S}$ -2MPA/ $\text{Fe}_3\text{O}_4$ )

Hybrid nanoparticles were prepared according to the method described in reference 47 (Picture 1). Briefly, lauric acid coating of  $\text{Fe}_3\text{O}_4$  nanoparticles suspended in chloroform was exchanged with the  $\text{Ag}_2\text{S}$ -2MPA NIRQDs, which transferred SPIONs into the aqueous phase [29]. Binding of external carboxylic acid groups of 2MPA of  $\text{Ag}_2\text{S}$  on  $\text{Fe}_3\text{O}_4$  surface triggers the hybrid structure formation. Use of excess amount of  $\text{Ag}_2\text{S}$ -2MPA forces the replacement of LA by carboxylates of  $\text{Ag}_2\text{S}$ -2MPA. 2MPA acts as a bifunctional ligand, at one end (thiol) attached to QD and on the other (carboxylic acid) to SPION crystal surfaces. These hybrid nanoparticles have a strong dark brown/black color, respond to external magnetic field and emit in the NIR region (Picture S1, Fig. 1). Absorbance and PL spectra of the hybrid nanoparticles resemble the absorbance and PL spectra of the corresponding  $\text{Ag}_2\text{S}$ -2MPA NIRQDs (Fig. S1, Fig. 1). There is a couple of nanometers shift in the emission maxima of the hybrid nanoparticles which can be expected in ligand exchange procedures. Although iron oxide does not have a significant absorbance in the NIR region, hybrids luminesce less than the corresponding NIRQDs. Luminescence decreases with increasing  $\text{Fe}_3\text{O}_4$  content. Table 1 shows the Ag/Fe ratio for all hybrids. H1 and H5 with Ag/Fe ratio of 14 and 13, respectively, retained about 70% and 60% of the luminescence intensity whereas others with Ag/Fe ratio less than 5 experienced a larger drop in the luminescence intensity (Fig. 1). A possible reason behind the drop in luminescence intensity is the absorbance of SPION at the excitation

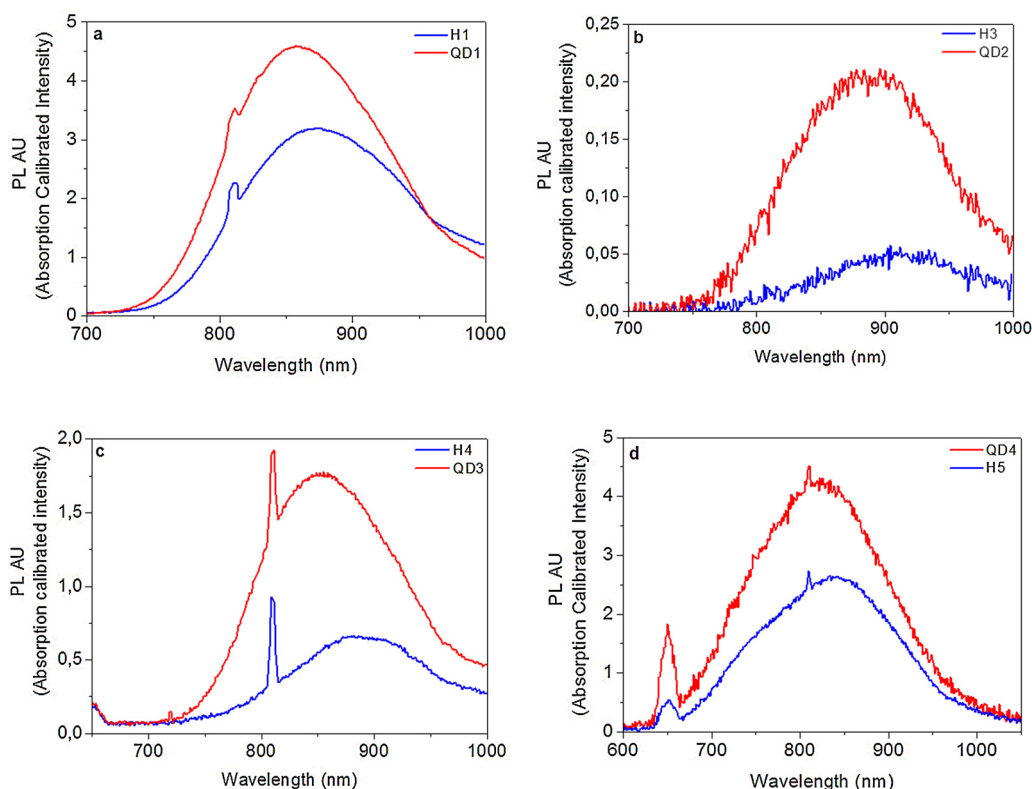


Fig. 1. PL spectra of  $\text{Ag}_2\text{S}$ -2MPA NIRQDs and the corresponding hybrid nanoparticles excited at 532 nm.

**Table 1**  
Properties of Ag<sub>2</sub>S NIRQDs and corresponding hybrid nanoparticles.

ID	Ag <sub>2</sub> S QDs	Ag <sub>2</sub> S <sup>a</sup> λ <sub>max</sub> (nm)	Ag <sub>2</sub> S FWHM (nm)	Hybrid Ag/Fe ratio <sup>b</sup> (nm)	Hybrid Dh <sup>c</sup> (nm)	Hybrid λ <sub>max</sub> <sup>a</sup> (nm)
H1	QD1	858	148	14	14(88)	873
H2	QD2	890	150	5	123(142)	– <sup>d</sup>
H3	QD2	890	150	3.5	42(220)	912
H4	QD3 <sup>e</sup>	863	165	2.2	23(57)	876
H5	QD4	825	204	13	24.7	840

<sup>a</sup> Excited at 532 nm.

<sup>b</sup> Mole ratio measured by ICP OES.

<sup>c</sup> Hydrodynamic size (diameter) measured by DLS and reported as number average and intensity based average in parenthesis, respectively.

<sup>d</sup> Could not be detected with Si detector.

<sup>e</sup> QD3: hydrodynamic size: 3.5 nm, zeta potential: –38 mV, quantum yield with respect to LDS 798 NIR dye: 39%.

wavelength (532 nm) (Fig. S2), surface perturbation of QDs that may cause non-radiative coupling, and concentration quenching due to high local concentration of QDs within the hybrid. When the luminescence intensity of Q4 and H5 were compared at an identical Ag concentration, it was seen that H5 does not have lower but actually higher luminescence intensity than Q4 (Fig. S3). This result indicates that, there is no significant damage done on QD surface during extraction/hybrid formation process which would cause loss in luminescence intensity. Sources of such effect can be a focus of another study.

Hydrodynamic size of Ag<sub>2</sub>S–2MPA NIRQDs measured by DLS (and reported as number average) is about 3.5 nm. Lauric acid coated SPIONs in chloroform are about 10 nm and hybrid nanoparticles composed of these two nanoparticles are about 25 nm with no size selective process (Table 1, Fig. S4). Although, there may be certain degree of error in sizes measured by DLS, the important information is the formation of a new entity of a larger size and that Ag<sub>2</sub>S–2MPA NIRQDs and SPIONs do not just coexist. Centrifugal Liquid Sedimentation (CLS) measurements are in good agreement with DLS analysis showing the absence of unconjugated Ag<sub>2</sub>S NIRQDs in the hybrid structure (Fig. S5). According to CLS, NIRQDs are 6.5 ± 3.6 nm in diameter whereas the hybrid nanoparticles are 12.8 ± 8.5 nm with a slightly wider size distribution. Both of these results confirm the ability of this preparation method in producing ultra-small hybrid nanoparticles. The measurement of Ag<sub>2</sub>S–2MPA NIRQDs by DLS (Z-average = 9.903 nm, PDI = 0.46) was employed to calculate the real density of the material (2.945 g/cm<sup>3</sup>) using the runtime of CLS (publication in progress). This apparent density is an average of a 3.3 nm of the hydration layer with a density of approximately 1 g/cm<sup>3</sup> and a core of 6.6 nm with a density of 7.4 g/cm<sup>3</sup>, which is consistent with TEM observations (Fig. S6). One should be aware of the inherent error introduced when measuring hybrid nanoparticles with this technique, since the density of Ag<sub>2</sub>S (7.23 g/cm<sup>3</sup>) was used as the density of the whole material.

XPS analyses of the hybrid nanoparticles (H4) confirmed the presence of both types of particles. Signals corresponding to the binding energies (BE) of Ag 3d, Fe 2p and S 2p core level with their abundance are given in Table S1. Typical Fe 2p signals of SPIONs at 710 eV and 726 eV [11] (Fig. S7b) shifted to 717 eV and 730 eV with a very low signal intensity complicating the fitting (Fig. S7a). Fe<sub>3</sub>O<sub>4</sub> particles are surrounded by Ag<sub>2</sub>S QDs which may be one of the possible reasons for the low signal. Ag 3d core level has spin–orbit coupling pair at BEs of 367.8 eV and 373.8 eV matching well with Ag<sub>2</sub>S (Fig. S7c) [32,41,42]. There are three types of sulfur based on the fittings of the signal obtained from S 2p: the one at 161 eV is usually assigned to S in the inorganic core (Ag<sub>2</sub>S) and the other one at 163 eV should belong to the sulfur of the coating material (2-MPA) (Fig. S7d) [32,43]. S 2p at BE of 162 eV is probably originating from the Ag<sub>2</sub>S with a different S-environment such as those closer to surface. If so, the ratio of Ag 3d to S 2p is about 2 which fits to chemical formula. Ag/Fe ratio found from XPS is 4.4/3 which is

significantly less than the ratio measured by ICP (H4, Table 1). Major source of the error in XPS is the poor signal of the Fe 2p which prevents accurate area analysis in XPS.

These hybrid nanoparticles are actually in the form of small clusters as can be seen in the TEM images (Fig. 2a and b). There are possibly two major reasons for such cluster formation: (1) the carboxylate surface of Ag<sub>2</sub>S NIRQDs may interact with multiple SPIONs simultaneously, (2) some clustering can take place during solvent evaporation on TEM grid. A range of different particles with average diameters between 3 and 10 nm can be seen in the TEM images. Different particle domains are distinguishable within these clusters, which is expected due to the presence of both Ag<sub>2</sub>S and Fe<sub>3</sub>O<sub>4</sub> nanoparticles (Fig. S8) which is also confirmed by the EDX analysis Fig. 2c–e. Although, presence of S and O seems to be distributed throughout the cluster due to existence of O and S in the coating molecule (2-MPA), slightly higher concentrations of S around Ag, and slightly higher concentrations of O around Fe can be seen in the images (Fig. 2c and d).

Magnetic properties of H3 and H4 were measured by VSM. Magnetization (*M*) with applied field (*H*) was measured at different temperatures (Fig. 3a and b). Field dependent magnetization curves (*M*–*H* curves) have S-shape at all temperatures. Magnetization sharply increases with the applied field, tend to saturate but not achieve full saturation at 15 kOe. This may mean higher fields are necessary for saturation and/or existence of some anti-ferromagnetic inter-cluster interactions mixed with ferromagnetic interactions within the clusters. Saturation magnetization of the hybrids can be found from the extrapolation of *M*–*H* curves (Table S2). H4 had higher *M*<sub>s</sub> compared to H3 since it contains more SPION. Hybrid nanoparticles did not show any hysteresis indicating superparamagnetism at and above 100 K (Fig. 3c and d). The separation between ZFC and FC curves indicate that there is a non-equilibrium magnetization below 100 K. The total magnetization of particles is nearly zero due to the random orientation of magnetic moments when the sample was cooled in zero magnetic field (ZFC situation). When an external magnetic field was applied (50 Oe), magnetic moments were reoriented along the applied magnetic field. With increasing temperature, orientation and hence, the magnetization increases reaching to a maximum at the blocking temperature, *T*<sub>B</sub>, which is about 100 K for these hybrid nanoparticles [44].

## 3.2. In vitro studies

### 3.2.1. Cytotoxicity and cellular uptake

Viability of HeLa and NIH/3T3 cells in contact with the hybrid nanoparticles were tested in 10–50 μg Ag/mL dose range in 24 h along with Silver Nitrate and QD1 and QD2 for comparison. Since each hybrid has a different SPION content, dosing could have been done in different ways but we have decided to use total Ag amount since Ag ion may be the most toxic component of the material. One should not forget that fixed Ag concentration would mean

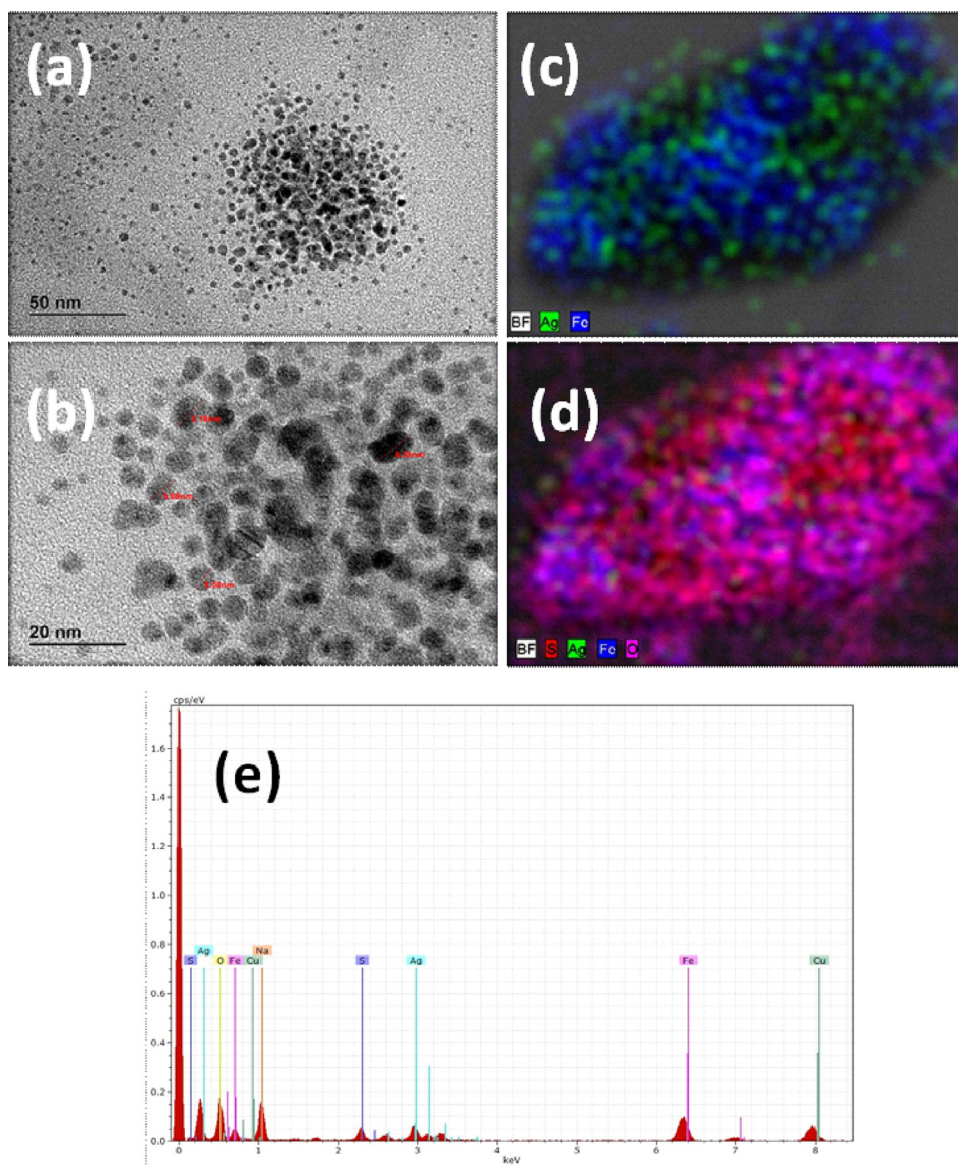


**Fig. 2.** TEM images of hybrid nanoparticles (A) 50 nm, (B) 20 nm scale. EDX analyses (C) Ag and Fe distribution, (D) Ag, S, Fe and O distribution by STEM images. (E) EDX energy transitions for the elements between 0 and 8 keV.

different particle concentrations and also different SPION loading. As can be seen in Fig. 4,  $\text{Ag}^+$  shows dose dependent toxicity and uptake (Fig. 4a and b and Fig. S9). Overall, nanoparticles were internalized more than  $\text{AgNO}_3$ , but are significantly more cyto-compatible in both cell lines, especially at high doses (25–50  $\mu\text{g}$   $\text{Ag}/\text{mL}$ ), also indicating stability of particles in the cells. In both cell lines, hybrid nanoparticles with smaller  $D_h$  (H1 and H4 with number average less than 30 nm and z-average less than 100 nm) are internalized significantly more than the larger ones. H1 is the smallest and the most internalized hybrid nanoparticle and showed no significant toxicity in HeLa at and below 25  $\mu\text{g}/\text{mL}$ , but viability dropped down to 80% at 50  $\mu\text{g}/\text{mL}$ . It is the most internalized nanoparticle by the NIH/3T3 cells as well, but in general, these cells are much more vulnerable than HeLa, and viability dropped down to 60% even at 10  $\mu\text{g}/\text{mL}$  and to 40% at 50  $\mu\text{g}/\text{mL}$ . H4 is the second most internalized nanoparticle by both cell lines. Although internalized more by HeLa, it showed no significant cytotoxicity within the studied dose range. On the other hand, dose dependent toxicity and less than 50% viability at the medium dose was seen in NIH/3T3. H1 and H4 are the smallest hybrid particles

with comparable emission maxima (Table 1). H4 has the highest Fe content and has the highest nanoparticle loading at the same time, but H1 has the lowest Fe content and the lowest nanoparticle loading. Total nanoparticle loading or Fe content seems to be negligible when compared with the size. The larger hybrid nanoparticles, H2 and H3 showed no significant dose dependent toxicity (around 80% viability) in HeLa with lower cell internalization (Fig. S9a). NIH/3T3 responded similarly to these two particles except viability dropped below 80% at the highest dose with H2 and below 60% with H3 which was internalized more compared to H2. Actually, H2 and H3, are the most cyto-compatible ones with NIH/3T3.

QD1, which is the  $\text{Ag}_2\text{S}$  used in the formation of H1, showed no statistically significant cytotoxicity compared to control (no nanoparticles) within the studied concentration range. When H1 and QD1 are compared, hybrid structure showed more toxicity but statistically significant difference was observed only at 50  $\mu\text{g}/\text{mL}$  indicating an influence of size and/or iron content on cyto-compatibility. Another interesting point is the extremely low level of QD1 uptake (0.7–0.8% at all doses), especially compared to H1 (45–18%).

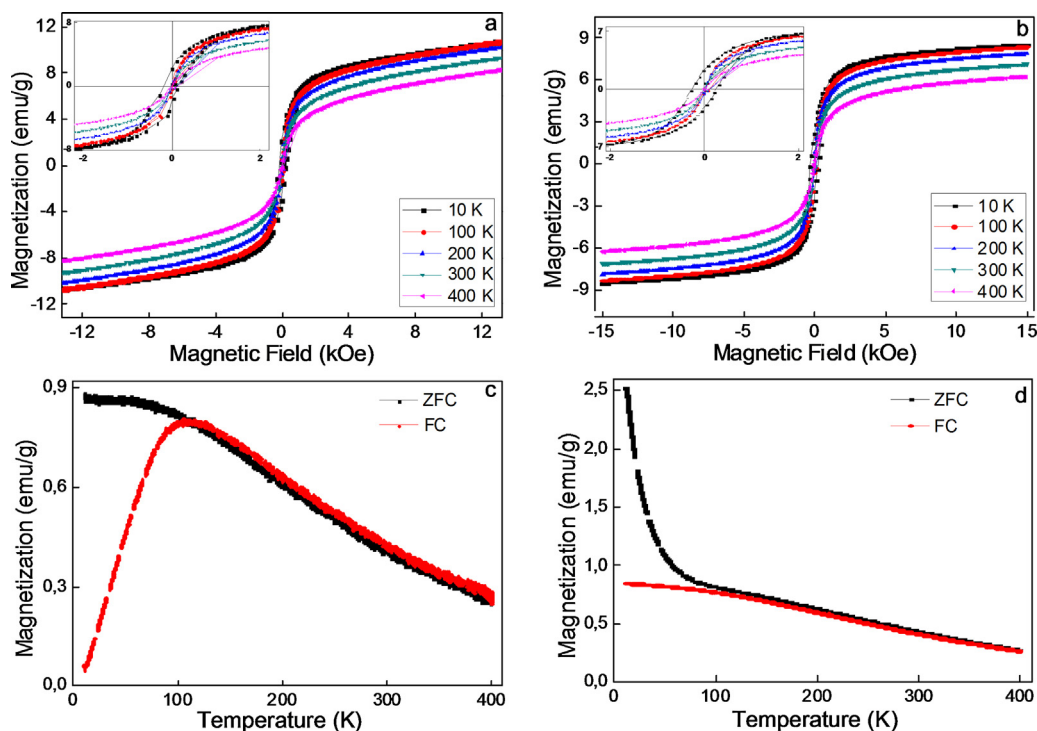


Fig. 3. *M*-*H* curves at different temperatures at  $\pm 15$  kOe for (a) H4 and (b) H3 sample. ZFC and FC (under 50 Oe) curves for (c) H4 and (d) H3.

H2 and H3 were made from QD2 which showed slightly better cyto-compatibility than its hybrids similar to QD1/H1 in NIH/3T3. Most significant difference is between QD2 and H3 at 50  $\mu\text{g}/\text{mL}$  with 97% and 55% viability, respectively.

### 3.2.2. Magnetic uptake

Presence of the magnetic nanoparticles within the hybrid structure provides opportunity for magnetic targeting. In order to study the influence of magnetic field on cell viability, H4 which is the

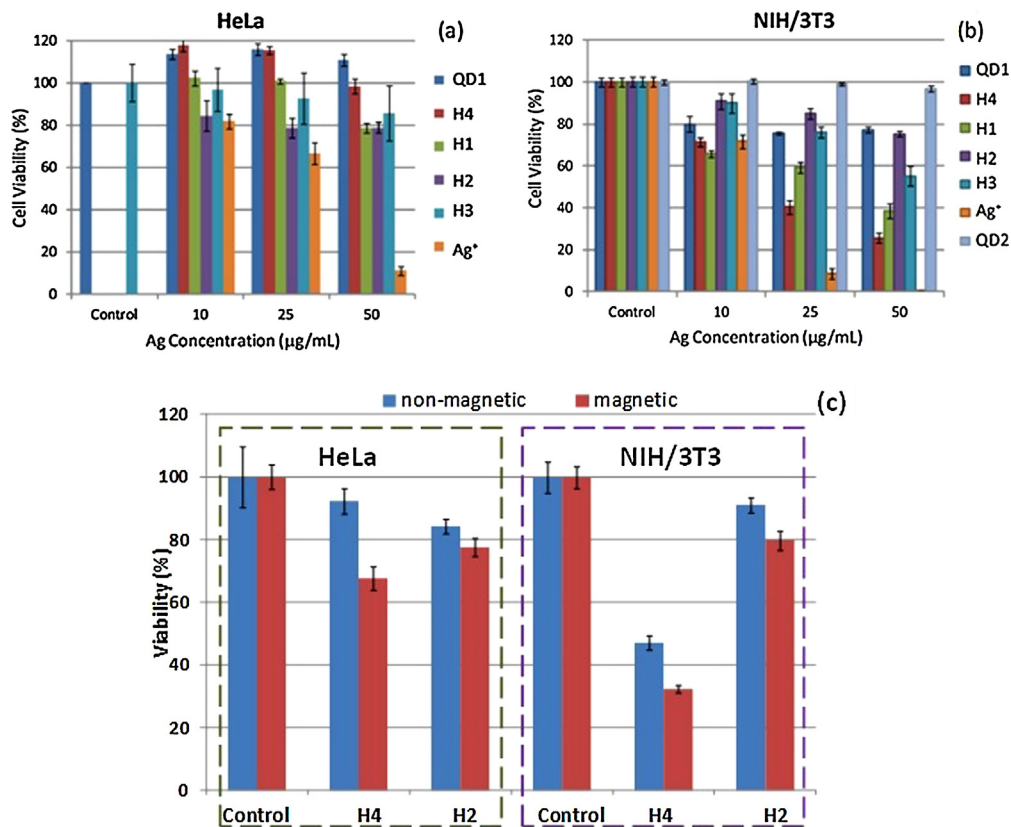
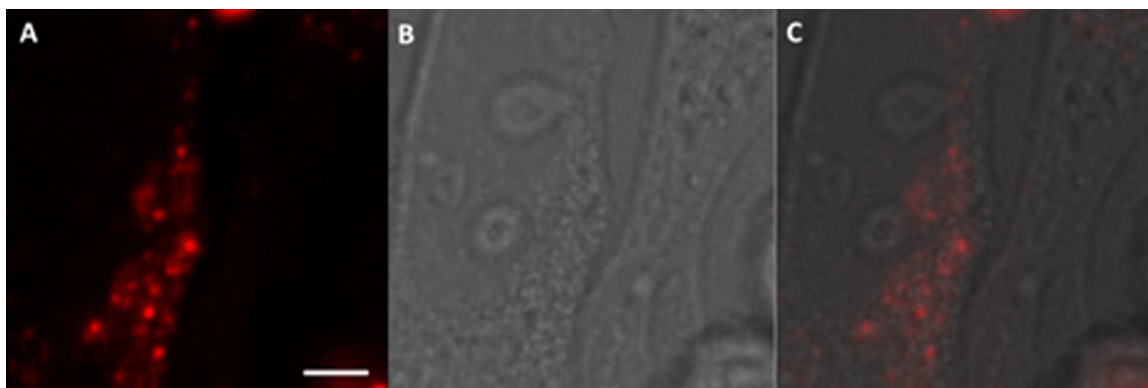


Fig. 4. (a, b) Change in the viability of (a) HeLa and (b) NIH/3T3 cells exposed to nanoparticles; (c) Change in the metabolic activity of HeLa and NIH/3T3 cells exposed to H2 and H4 nanoparticles in the absence and presence of magnetic field at 25  $\mu\text{g}/\text{mL}$  dose. Viability was determined by MTT assay after 24 h exposure to nanoparticles.



**Fig. 5.** Confocal laser scanning micrographs of hybrid nanoparticles localized in HeLa cells (50  $\mu\text{g}/\text{mL}$  hybrid incubated for 6 h). (A) Fluorescence, (B) transmission, (C) overlay images. The scale bar represents 5  $\mu\text{m}$ .

**Table 2**

Summary of the hemocompatibility data of the hybrid nanoparticles, H4 and H5, and of their corresponding controls.<sup>g</sup>

ID	Blood cell reaction				Humoral reaction		
	RBC's/ $\mu\text{L}$ ( $10\text{E}^6$ )	Platelets/ $\mu\text{L}$ ( $10\text{E}^3$ )	WBC's/ $\mu\text{L}$	Hemolysis (%) <sup>a</sup>	Intrinsic coagulation (%) <sup>f</sup>	Extrinsic coagulation (%) <sup>f</sup>	Complement activation (%)
H4	98.6 $\pm$ 0.5	114.2 $\pm$ 1.4	97.4 $\pm$ 2.0	0.4 $\pm$ 0.1	100 $\pm$ 2	114 $\pm$ 4	118 $\pm$ 4
H5	99.8 $\pm$ 0.4	116.1 $\pm$ 1.5	96.7 $\pm$ 1.2	0.5 $\pm$ 0.1	52 $\pm$ 3	52 $\pm$ 2	148 $\pm$ 5
QD4	100.2 $\pm$ 0.2	115.5 $\pm$ 7.8	97.4 $\pm$ 3.5	0.5 $\pm$ 0.1	73 $\pm$ 3	81 $\pm$ 2	103 $\pm$ 1
SPION	99.4 $\pm$ 0.6	116.6 $\pm$ 3.1	99.3 $\pm$ 2.0	0.9 $\pm$ 0.1	100 $\pm$ 1	>130	212 $\pm$ 4
2MPA	99.5 $\pm$ 0.4	108.0 $\pm$ 4.0	98.0 $\pm$ 1.2	0.6 $\pm$ 0.1	100 $\pm$ 3	117 $\pm$ 4	91 $\pm$ 1
+Ctrl	–	–	–	40.3 $\pm$ 0.1 <sup>b</sup>	74 $\pm$ 2 <sup>c</sup>	>130 <sup>c</sup>	154 $\pm$ 4
Ctrl I <sup>d</sup>	98.6 $\pm$ 0.9	112.7 $\pm$ 8.6	94.0 $\pm$ 1.2	0.6 $\pm$ 0.1	100 $\pm$ 2	109 $\pm$ 2	100 $\pm$ 4
Ctrl NI <sup>e</sup>	100.0 $\pm$ 0.4	100.0 $\pm$ 2.9	100 $\pm$ 1.1	0.3 $\pm$ 0.1	100 $\pm$ 4	109 $\pm$ 3	98 $\pm$ 5

<sup>a</sup> According to ASTM F 756-00: <2% is considered as non-hemolytic; 2% < x < 5% is slightly hemolytic; >5% hemolytic.

<sup>b</sup> Saponin.

<sup>c</sup> Kaolin.

<sup>d</sup> Ctrl I: blood control incubated.

<sup>e</sup> Ctrl NI: blood control non-incubated.

<sup>f</sup> Clotting ability of the standard plasma is assumed to be 100%. The longer it takes plasma to clot, the lower is its clotting ability, and the lower is the resulting test value expressed in percent to the standard plasma. Therefore a reduction of the % corresponds to an inactivation of this coagulation pathway.

<sup>g</sup> Final concentration in the whole blood = 100  $\mu\text{g}/\text{mL}$ .

least toxic hybrid to HeLa but most toxic to NIH/3T3, and H2 which is the least toxic hybrid to NIH/3T3 and most toxic to HeLa were incubated with cells at 25  $\mu\text{g}/\text{mL}$  Ag concentration for 24 h. H4 showed more significant decrease in the cell viability in magnetic field in both cell lines which is reasonable since it has more SPION in the hybrid than H2 (Ag/Fe = 2 versus Ag/Fe = 5.1) (Fig. 4c, Fig. S10). Higher SPION content provides more effective magnetic response and more uptake.

### 3.2.3. In vitro cellular imaging

Confocal laser scanning micrographs reveal that hybrids were successfully internalized by the HeLa cells due to the strong signal received from the QD part of the hybrid nanoparticles (Fig. 5). Autofluorescence can be observed from the untreated sample cells (Fig. S11A) but this is completely diminished in the presence of strong NIR signal monitored in the cytoplasm of the cells (Fig. 5 and Fig. S11B). No hybrids were observed in the nucleus which is usual for cellular uptake of most QDs (Fig. S12).

### 3.2.4. Hemocompatibility

In the frame of this study, hemocompatibility of two representative hybrid nanoparticles H4 and H5 have been assessed (Table 2). In order to differentiate the effect of the individual components of these hybrids, QD4, SPION, 2MPA as well as the usual negative and positive controls were used to judge the reactivity of the biological cascades. The main difference that would impact the hemoreactivity between these two hybrid nanoparticles is the Ag<sub>2</sub>S/SPION ratio, i.e. Ag/Fe mole ratio of 2.2 in H4 and 13 in H5, corresponding to

significantly higher QD content in H5 nanoparticles. All samples have been assessed at three concentrations in the blood, i.e. 1, 10 and 100  $\mu\text{g}/\text{mL}$  (final concentration in the whole blood). However, for the sake of clarity, only the results obtained at 100  $\mu\text{g}/\text{mL}$  are given in Table 2, since some reactivity of the blood has been observed only at this highest sample concentration.

The first series of tests dedicated to the blood cellular response (Table 2) revealed good hemotolerance in relation to major cellular components of the blood. Amongst them hemolysis (or red blood cell lysis) is the most popular parameter adopted by the authors. These two hybrid nanoparticles caused no significant hemolysis, no change in size or count of red blood cells within the studied dose range (1  $\mu\text{g}/\text{mL}$  to 100  $\mu\text{g}/\text{mL}$ ). This is somewhat expected since most of the synthetic solid materials do not affect the integrity of erythrocytes which are mostly sensitive to compounds with amphiphilic behavior or able to neutralize the surface charges of glycocalyx, such as polycations. However, this observation is particularly valuable for platelets which are typically more reactive to foreign body surfaces, inducing their activation or/and aggregation. Indeed, the absence of platelet aggregation testifies their potential as intravenous formulations.

Meanwhile, hybrid nanoparticles displayed a significant level of intervention with the two interlinked protective systems of complement activation and blood coagulation at the 100  $\mu\text{g}/\text{mL}$  dose. Noteworthy, when tested *in vitro* under the same conditions as the 2MPA and negative controls, H5 induced a significant inhibition of the two coagulation tests (coagulation time reduced to 52%) with a  $\sim$ 1.5 times increase in C3a assay (columns 6–8 of Table 2).

Interestingly, H4 did not interfere with the coagulation (higher SPION content), not more than on the complement, whilst SPION alone increased drastically and selectively the extrinsic pathway of the homeostasis, and activated the immune part of the complement by more than a factor of two.

Interpretation of these findings may be too speculative without further investigation of protein–material interactions but, at this stage it seems nevertheless reasonable to assume that the different inhibitions observed on the coagulation pathways should find their origin in a selective interactions between various protein factors and nanoparticle surface at the stage of sample pre-incubation with blood, leading to a lack of availability of the free and intact protein. Indeed, a commonplace truth is that immediately upon mixing with blood, nanoparticles acquire a protein corona through opsonization [45]. As a consequence, even a slight decrease in plasma protein concentration may cause a shift in the equilibrium of cascade reactions. It is also well-known that even non-specific deposition of C3 on some polymer surfaces causes conformational changes followed by the initiation of C3 convertase formation in the presence of factors B and D, thus increase the alternative pathway turnover [46]. A mean negative zeta potential, but also differences in patterns of charge distribution, should certainly promote and explain variations in binding of plasma proteins which are abundant in positively charged residues, e.g., coagulation factor XII and high molecular weight kininogen [47], or a polipoprotein H [48].

#### 4. Conclusions

Aqueous Ag<sub>2</sub>S NIRQDs which has been shown as non-toxic [32] without any inorganic shell formation or PEGylation are excellent candidates for *in vitro* and *in vivo* studies where optical imaging and drug/gene delivery is required. SPIONs, which are biocompatible MRI contrast agents, are also evaluated in magnetic targeting, hyperthermia as well as drug delivery in the *in vitro* studies. Combination of the two (SPION and Ag<sub>2</sub>S NIRQDs) in a nanoscale hybrid structure is very valuable for biotechnology and medicine. Hybrids composed of SPION and Ag<sub>2</sub>S were prepared by a straight forward ligand exchange method, to combine the unique properties of both in a single entity. For the hybrid formation, lauric acid coated SPIONs in chloroform and 2-MPA coated aqueous Ag<sub>2</sub>S NIRQDs were mixed. Carboxylic acid of 2-MPA replaced LA on the SPION surface and dragged SPIONs into the aqueous phase. Based on DLS, CLS and TEM analysis these hybrids are small clusters (sizes mostly less than 150 nm) composed of multiple SPIONs and QDs. Hybrid nanoparticles with distinctly different emission wavelengths (*ca* 840, 870, 910 nm), small size, colloidal stability and high luminescence intensity with ferro-fluidic behavior in magnetic field were obtained. Slight red shift and a decrease in emission intensity with respect to emission maxima and intensity of the corresponding QDs may be due to several reasons including surface perturbation during ligand exchange and absorption of photons at the excitation wavelength by SPIONs. *M–H* curves indicated superparamagnetic behavior for the hybrid nanoparticles. Higher saturation magnetization is observed with increasing Fe content of the hybrid structures, so, response to magnetic field can be tailored by the iron content of the hybrids.

*In vitro* cytotoxicity and cellular uptake studies at doses as high as 50 µg Ag/mL in both HeLa and NIH/3T3 cell lines were determined. Overall, hydrodynamic size of the hybrids is a significant factor affecting the cell viability and showed difference in different cell lines. Small sized particles were internalized more by both cell lines and even more by NIH/3T3 and are more toxic in NIH/3T3 cells. Larger particles were tolerated better by the NIH/3T3 but smaller ones were more cytocompatible in HeLa. In general, NIH/3T3 cells seem to be more vulnerable to nanoparticles. HeLa cells showed at

and above 80% viability in the presence of all particles at all doses. The origin of such behavior is a subject of a different study where probably internalization pathways and protein corona are studied. Existence of SPIONs in the hybrid composition was utilized in magnetic targeting of hybrid nanoparticles in the *in vitro* studies. Cell viability decreased in the presence of external magnetic field with the particles having more Fe content due to better response to magnetic field, increasing the contact of cells with hybrid nanoparticles and therefore the cell internalization.

The panel of hemocompatibility tests reported here has proved a relatively good hemotolerance of the hybrid nanoparticles. Some of the side reactions noticed regarding coagulation and complement activation at the 100 µg/mL dose should draw more attention in the future, especially for the *in vivo* exploitation of such formulations. Exact mechanism of blood–nanoparticle interaction may be identified in further studies. Yet, this is the first report on hemocompatibility of such hybrid structures.

In addition, hybrid nanoparticles were successfully used in imaging HeLa cells. A great advantage of using a NIRQD in eliminating background signal in CLM was clearly seen. Particles showed strong luminescence intensity, cytoplasmic distribution and no nuclear uptake.

Overall, in a very simple preparation method, magnetic and luminescent hybrid nanoparticles composed of SPION and Ag<sub>2</sub>S-NIRQDs were prepared in small size regime with colloidal and optical stability, good cyto and hemocompatibility, strong luminescence and response to magnetic field. All these characteristics suggest a great potential as new theranostic nanoparticles.

#### Acknowledgements

Authors thank Dr. Ugur Unal (KUYTAM, Koc University) for XPS analysis and Dr. Özgür Birer (Koc University, Department of Chemistry) for the construction of home made spectrofluorometer.

#### Appendix A. Supplementary data

Supplementary data associated with this article can be found, in the online version, at <http://dx.doi.org/10.1016/j.colsurfb.2015.05.051>

#### References

- [1] A. Singh, S.K. Sahoo, Magnetic nanoparticles: a novel platform for cancer theranostics, *Drug Discov. Today* 19 (4) (2014) 474–481.
- [2] S. Hasan Hussein-Al-Ali, P. Arulselvan, S. Fakurazi, M.Z. Hussein, D. Dorniani, Arginine–chitosan- and arginine–polyethylene glycol-conjugated superparamagnetic nanoparticles: preparation, cytotoxicity and controlled-release, *J. Biomater. Appl.* (2014).
- [3] Y. Cohen, S.Y. Shoushan, Magnetic nanoparticles-based diagnostics and theranostics, *Curr. Opin. Biotechnol.* 24 (2013) 672–681.
- [4] C. Nazli, G.S. Demirel, Y. Yar, H.Y. Acar, S. Kizilel, Targeted delivery of doxorubicin into tumor cells via MMP-sensitive PEG hydrogel-coated magnetic iron oxide nanoparticles (MIONPs), *Colloids Surf. B: Biointerfaces* 122 (2014) 674–683.
- [5] H.Y. Acar, R. Kas, E. Yurtsever, C. Ozen, I. Lieberwirth, Emergence of 2MPA as an effective coating for highly stable and luminescent quantum dots, *J. Phys. Chem. C* 113 (2009) 10005–10012.
- [6] H.M.E. Azzazy, M.M.H. Mansour, S.C. Kazmierczak, From diagnostics to therapy: prospects of quantum dots, *Clin. Biochem.* 40 (2007) 917–927.
- [7] P.P. Ghoroghchian, M.J. Therien, D.A. Hammer, *In vivo* fluorescence imaging: a personal perspective, *Wiley Interdiscip. Rev. Nanomed. Nanobiotechnol.* 1 (2009) 156–167.
- [8] A.K. Gupta, M. Gupta, Synthesis and surface engineering of iron oxide nanoparticles for biomedical applications, *Biomaterials* 26 (2005) 3995–4021.
- [9] J.E. Rosen, L. Chan, D.-B. Shieh, F.X. Gu, Iron oxide nanoparticles for targeted cancer imaging and diagnostics, *Nanomed. Nanotechnol. Biol. Med.* 8 (2012) 275–290.
- [10] T.K. Jain, J. Richey, M. Strand, D.L. Leslie-Pelecky, C.A. Flask, V. Labhasetwar, Magnetic nanoparticles with dual functional properties: drug delivery and magnetic resonance imaging, *Biomaterials* 29 (2008) 4012–4021.

- [11] H. Maleki, A. Simchi, M. Imani, B.F.O. Costa, Size-controlled synthesis of superparamagnetic iron oxide nanoparticles and their surface coating by gold for biomedical applications, *J. Magn. Magn. Mater.* 324 (2012) 3997–4005.
- [12] V. Biju, S. Mundayoor, R.V. Omkumar, A. Anas, M. Ishikawa, Bioconjugated quantum dots for cancer research: present status, prospects and remaining issues, *Biotechnol. Adv.* 28 (2010) 199–213.
- [13] E.I. Altinoğlu, J.H. Adair, Near infrared imaging with nanoparticles, *Wiley Interdiscip. Rev. Nanomed. Nanobiotechnol.* 2 (2010) 461–477.
- [14] J. Gao, K. Chen, R. Xie, J. Xie, Y. Yan, Z. Cheng, X. Peng, X. Chen, In vivo tumor-targeted fluorescence imaging using near-infrared non-cadmium quantum dots, *Bioconjug. Chem.* 21 (2010) 604–609.
- [15] A. Guchhait, A.K. Rath, A.J. Pal, To make polymer: quantum dot hybrid solar cells NIR-active by increasing diameter of PbS nanoparticles, *Sol. Energy Mater. Sol. Cells* 95 (2011) 651–656.
- [16] I. Gur, N.A. Fromer, M.L. Geier, A.P. Alivisatos, Air-stable all-inorganic nanocrystal solar cells processed from solution, *Science* 310 (2005) 462–465.
- [17] I. Robel, V. Subramanian, M. Kuno, P.V. Kamat, Quantum dot solar cells. Harvesting light energy with CdSe nanocrystals molecularly linked to mesoscopic TiO<sub>2</sub> films, *J. Am. Chem. Soc.* 128 (2006) 2385–2393.
- [18] W.C.W. Chan, D.J. Maxwell, X. Gao, R.E. Bailey, M. Han, S. Nie, Luminescent quantum dots for multiplexed biological detection and imaging, *Curr. Opin. Biotechnol.* 13 (2002) 40–46.
- [19] J. Ou, F. Wang, Y. Huang, D. Li, Y. Jiang, Q.-H. Qin, Z.H. Stachurski, A. Tricoli, T. Zhang, Fabrication and cyto-compatibility of Fe<sub>3</sub>O<sub>4</sub>/SiO<sub>2</sub>/graphene-CdTe QDs/CS nanocomposites for drug delivery, *Colloids Surf. B: Biointerfaces* 117 (2014) 466–472.
- [20] J. Zhu, Y. Lu, Y. Li, J. Jiang, L. Cheng, Z. Liu, L. Guo, Y. Pan, H. Gu, Synthesis of Au-Fe<sub>3</sub>O<sub>4</sub> heterostructured nanoparticles for in vivo computed tomography and magnetic resonance dual modal imaging, *Nanoscale* 6 (2014) 199–202.
- [21] J. Zhu, B. Zhang, J. Tian, J. Wang, Y. Chong, X. Wang, Y. Deng, M. Tang, Y. Li, C. Ge, Y. Pan, H. Gu, Synthesis of heterodimer radionuclide nanoparticles for magnetic resonance and single-photon emission computed tomography dual-modality imaging, *Nanoscale* 7 (2015) 3392–3395.
- [22] L.M. Lacroix, F. Delpech, C. Nayral, S. Lachaize, B. Chaudret, New generation of magnetic and luminescent nanoparticles for in vivo real-time imaging, *Interface Focus* 3 (2013).
- [23] A. Abdulkayum, C.-X. Yang, Q. Zhao, J.-T. Chen, L.-X. Dong, X.-P. Yan, Gadolinium complexes functionalized persistent luminescent nanoparticles as a multimodal probe for near-infrared luminescence and magnetic resonance imaging in vivo, *Anal. Chem.* 86 (2014) 4096–4101.
- [24] K.D. Nisha, M. Navaneethan, B. Dhanalakshmi, K. Saravana Murali, Y. Hayakawa, S. Ponnusamy, C. Muthamizhchelvan, P. Gunasekaran, Effect of organic-ligands on the toxicity profiles of CdS nanoparticles and functional properties, *Colloids Surf. B: Biointerfaces* 126 (2015) 407–413.
- [25] J.-M. Shen, X.-M. Guan, X.-Y. Liu, J.-F. Lan, T. Cheng, H.-X. Zhang, Luminescent/magnetic hybrid nanoparticles with folate-conjugated peptide composites for tumor-targeted drug delivery, *Bioconjug. Chem.* 23 (2012) 1010–1021.
- [26] R. Xie, K. Chen, X. Chen, X. Peng, InAs/InP/ZnSe core/shell/shell quantum dots as near-infrared emitters: bright, narrow-band, non-cadmium containing, and biocompatible, *Nano Res.* 1 (2008) 457–464.
- [27] R. Aswathy, Y. Yoshida, T. Maekawa, D. Kumar, Near-infrared quantum dots for deep tissue imaging, *Anal. Bioanal. Chem.* 397 (2010) 1417–1435.
- [28] S.B. Rizvi, S. Ghaderi, M. Keshtgar, A.M. Seifalian, Semiconductor quantum dots as fluorescent probes for in vitro and in vivo bio-molecular and cellular imaging, *Nano Rev.* 1 (2010).
- [29] R. Kas, E. Sevinc, U. Topal, H.Y. Acar, A universal method for the preparation of magnetic and luminescent hybrid nanoparticles, *J. Phys. Chem. C* 114 (2010) 7758–7766.
- [30] H. Wang, J. Shen, Y. Li, Z. Wei, G. Cao, Z. Gai, K. Hong, P. Banerjee, S. Zhou, Magnetic iron oxide-fluorescent carbon dots integrated nanoparticles for dual-modal imaging, near-infrared light-responsive drug carrier and photothermal therapy, *Biomater. Sci.* 2 (2014) 915–923.
- [31] H. Chen, B. Qi, T. Moore, D.C. Colvin, T. Crawford, J.C. Gore, F. Alexis, O.T. Mefford, J.N. Anker, Synthesis of brightly PEGylated luminescent magnetic upconversion nanophosphors for deep tissue and dual MRI imaging, *Small* 10 (2014) 160–168.
- [32] I. Hocaoglu, M.N. Cizmeciyan, R. Erdem, C. Ozen, A. Kurt, A. Sennaroglu, H.Y. Acar, Development of highly luminescent and cytocompatible near-IR-emitting aqueous Ag<sub>2</sub>S quantum dots, *J. Mater. Chem.* 22 (2012) 14674–14681.
- [33] Y. Zhang, G. Hong, Y. Zhang, G. Chen, F. Li, H. Dai, Q. Wang, Ag<sub>2</sub>S quantum dot: a bright and biocompatible fluorescent nanoprobe in the second near-infrared window, *ACS Nano* 6 (2012) 3695–3702.
- [34] G. Chen, F. Tian, Y. Zhang, Y. Zhang, C. Li, Q. Wang, Tracking of transplanted human mesenchymal stem cells in living mice using near-infrared Ag<sub>2</sub>S quantum dots, *Adv. Funct. Mater.* 24 (2014) 2481–2488.
- [35] Y. Hua-Yan, Z. Yu-Wei, Z. Zheng-Yong, X. Huan-Ming, Y. Shao-Ning, One-pot synthesis of water-dispersible Ag<sub>2</sub>S quantum dots with bright fluorescent emission in the second near-infrared window, *Nanotechnology* 24 (2013) 055706.
- [36] N. Won, S. Jeong, K. Kim, J. Kwag, J. Park, S.G. Kim, S. Kim, Imaging depths of near-infrared quantum dots in first and second optical windows, *Mol. Imaging* 11 (2012) 338–352.
- [37] H. Zhao, K. Saatchi, U.O. Häfeli, Preparation of biodegradable magnetic microspheres with poly(lactic acid)-coated magnetite, *J. Magn. Magn. Mater.* 321 (2009) 1356–1363.
- [38] B.I. Cerda-Cristerna, H. Flores, A. Pozos-Guillén, E. Pérez, C. Sevrin, C. Grandfils, Hemocompatibility assessment of poly(2-dimethylamino ethyl-methacrylate) (PDMAEMA)-based polymers, *J. Control. Release* 153 (2011) 269–277.
- [39] I. Hocaoglu, F. Demir, O. Birer, A. Kiraz, C. Sevrin, C. Grandfils, H. Yagci Acar, Emission tunable, cyto/hemocompatible, near-IR-emitting Ag<sub>2</sub>S quantum dots by aqueous decomposition of DMSA, *Nanoscale* 6 (2014) 11921–11931.
- [40] N.R. Kuznetsova, C. Sevrin, D. Lespineux, N.V. Bovin, E.L. Vodovozova, T. Mészáros, J. Szabeni, C. Grandfils, Hemocompatibility of liposomes loaded with lipophilic prodrugs of methotrexate and melphalan in the lipid bilayer, *J. Control. Release* 160 (2012) 394–400.
- [41] B. Vincent Christ, *Handbook of the Elements and Native Oxides*, Wiley-Blackwell, 1999.
- [42] R.B.C. Orléans, 2012, <http://www.lasurface.com/database/elementxps.php>
- [43] C. Rui, T.N. Noel, M. Laura, R.M. Hannah, M.W. Paul, Silver sulfide nanoparticle assembly obtained by reacting an assembled silver nanoparticle template with hydrogen sulfide gas, *Nanotechnology* 19 (2008) 455604.
- [44] M. Sertkol, Y. Koseoglu, A. Baykal, H. Kavas, M.S. Toprak, Synthesis and magnetic characterization of Zn<sub>0.7</sub>Ni<sub>0.3</sub>Fe<sub>2</sub>O<sub>4</sub> nanoparticles via microwave-assisted combustion route, *J. Magn. Magn. Mater.* 322 (2010) 866–871.
- [45] P. Aggarwal, J.B. Hall, C.B. McLeland, M.A. Dobrovolskaia, S.E. McNeil, Nanoparticle interaction with plasma proteins as it relates to particle biodistribution, biocompatibility and therapeutic efficacy, *Adv. Drug Deliv. Rev.* 61 (2009) 428–437.
- [46] S.M. Moghimi, A.J. Andersen, D. Ahmadvand, P.P. Wibroe, T.L. Andresen, A.C. Hunter, Material properties in complement activation, *Adv. Drug Deliv. Rev.* 63 (2011) 1000–1007.
- [47] B.J. Clarke, H.C. Côté, D.E. Cool, I. Clark-Lewis, H. Saito, R.A. Pixley, R.W. Colman, R.T. MacGillivray, Mapping of a putative surface-binding site of human coagulation factor XII, *J. Biol. Chem.* 264 (1989) 11497–11502.
- [48] R. Schwarzenbacher, K. Zeth, K. Diederichs, A. Gries, G.M. Kostner, P. Laggner, R. Prassl, Crystal structure of human β<sub>2</sub>-glycoprotein I: implications for phospholipid binding and the antiphospholipid syndrome, *EMBO J.* 18 (22) (1999) 6228–6239.